# Mononuclear Ruthenium-Based Water Oxidation Catalyst Supported by Anionic, Redox-Non-Innocent Ligand: Heterometallic O−O Bond Formation via Radical Coupling Pathway

Animesh Kundu,[∥] Suman Kr Dey,[∥] Subhasis Dey,[∥] Anakuthil Anoop,*[ID] and Sukanta Mandal*[ID]

Department of Chemistry, Indian Institute of Technology Kharagpur, Kharagpur 721302, India
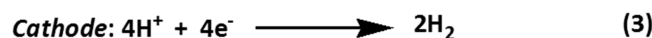
S *Supporting Information*

ABSTRACT: Cerium(IV)-driven water oxidation catalysis mediated by a mononuclear ruthenium(III) complex, $[Ru(L)(pic)_3]$ (H_3L = 2,2′-iminodibenzoic acid, pic = 4-methylpyridine), has been demonstrated in this work. The mechanistic details of water oxidation have been investigated by the combined use of spectroscopy, electrochemistry, kinetic analysis, and computational studies. It was found that water oxidation proceeds via formal high-valent Ru^{VII} species. The capability of accessing such a high-valent state is derived from the non-innocent behavior of the anionic tridentate ligand frame which helps in accumulation of oxidative equivalents in cooperation with metal center. This metal−ligand cooperation facilitates the multi-electron-transfer reaction such as water oxidation. Kinetic analysis suggests water oxidation at a single site of Ru where O−O bond formation occurs via radical−radical coupling pathway between the oxygen atom of ruthenium-oxo species and the oxygen atom of the hydroxocerium(IV) ion.
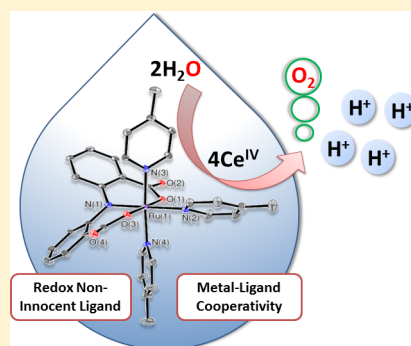
INTRODUCTION

The production of hydrogen by the light-driven splitting of water in an artificial photosynthesis device is a promising strategy to develop carbon-free, environmentally friendly, and sustainable energy economy. The photo splitting of water (eq 1) consists of three major chemical processes, viz., light harvesting and charge separation, water oxidation, and proton reduction. The light-harvesting chromophores capture light and generate holes which promote $4e^-$ oxidation of two water molecules in the presence of water oxidation catalyst (WOC) at the anode to generate O_2 and protons (eq 2). In the cathode reaction, protons generated at the anode are reduced in the presence of proton reduction catalyst to produce H_2 gas (eq 3). Thus, to generate H_2 fuel from water in an artificial photosystem device, all these reactions should occur concurrently in an efficient manner.[1−4]

$$2H_2O \xrightarrow{\ h\nu\ } 2H_2 + O_2 \qquad (1)$$

$$\textit{Anode}: 2H_2O \longrightarrow O_2 + 4H^+ + 4e^- \qquad (2)$$

$$\textit{Cathode}: 4H^+ + 4e^- \longrightarrow 2H_2 \qquad (3)$$

Currently, the water oxidation step (eq 2) is the bottleneck to fabricate an efficient artificial photosystem device, since it is an energetically uphill process with enormous complexity involving the transfer of multiple protons and electrons along with slow kinetics of an oxygen−oxygen (O−O) bond formation.[1,5] To overcome these challenges, understanding of the water oxidation step at the molecular level and finding an efficient WOC are very crucial in order to build up an efficient

artificial photosystem device for generation of solar fuel such as H_2 from water.

Considerable progress has been made during the past years with the development of molecular WOCs based on precious metals (Ru and Ir)[1] and earth-abundant first-row transition metal ions;[6] among these, Ru-based WOCs[7−17] have attracted much attention because of their versatile redox properties, superior catalytic performance, and higher stability. In recent years, focus has been diverted toward the design of single-site WOCs[10−17] because of their facile synthesis and less complexity in the mechanistic investigation. Over the past few years, tremendous efforts with both experimental and theoretical studies have been devoted in order to understand the mechanism of water oxidation mediated by molecular WOCs, particularly the critical O−O bond forming event. Two pathways have been proposed for O−O bond formation: (i) water nucleophilic attack at electron-deficient oxo group of a high-valent metal-oxo unit (WNA pathway) and (ii) radical O−O coupling interaction between two metal-oxyl units (I2M pathway).[18] A third pathway has been proposed for few instances where O−O bond formation occurs via radical coupling interaction between the oxygen atom of a hydroxocerium(IV) ion ($Ce^{IV}-OH$) and a metal oxyl unit (I2M−HC), when ceric ammonium nitrate (CAN) has been used as sacrificial oxidant (Scheme 1).[15]

To design an efficient water oxidation catalyst, it is essential that metal complexes should be able to reach a high oxidation state at a narrow potential window with nominal overpotential

Scheme 1. Depiction of Different O—O Bond Formation Pathways
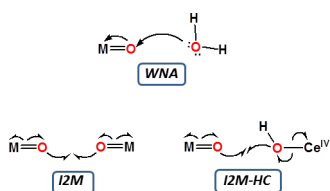
and be able to survive under a highly oxidizing condition. Nature performs water oxidation efficiently at the oxygen-evolving complex (OEC) of photosystem II which consists of a Mn_4CaO_5 cluster surrounded by negatively charged oxo and carboxylate ligands.[19] These negatively charged donor groups strongly stabilize the high-valent states of the Mn cluster via extensive electron donation and play vital roles in effective water oxidation catalysis with low over potential. Therefore, incorporation of negatively charged donor groups into the ligand scaffold would be a promising approach to design a molecular WOC. In addition to this, if a ligand actively participates in the redox reaction, then a metal—ligand cooperative effect might assist the multi-electron-transfer process, as observed before.[9,12] Furthermore, water ligation in a metal complex would promote the proton-coupled electron-transfer (PCET) process which would help to avoid build-up of Coulombic charge.[10] Thus, it is anticipated that the presence of all three features in a catalyst might be helpful for multi-electron-transfer reaction such as water oxidation.

With these considerations in mind, we developed a mononuclear complex, $[Ru(L)(pic)_3]$ (**1-Ru^{III}**) (Scheme 2),

Scheme 2. Molecular Structure of Complex $[Ru(L)(pic)_3]$ (1-Ru^{III})
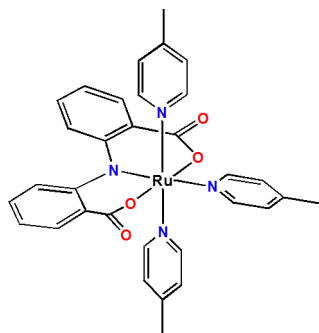
supported by tridentate anionic ligand L^{3-} (H_3L = 2,2′-iminodibenzoic acid) and three 4-methylpyridine (pic) moieties, as precatalyst for the water oxidation reaction. Herein we report the synthesis and structural, spectroscopic, and electrochemical characterization of complex **1-Ru^{III}**, together with its ability toward Ce^{IV}-driven oxidation of water to dioxygen under acidic condition. We further explored the mechanism details for water oxidation using both experimental and computational studies. Electrochemical studies suggest the generation of a high-valent formal ruthenium(VII)-oxo intermediate which triggers the water oxidation process. The observed features of accessing such a high-valent state are a consequence of the strong electron-donating property of the anionic ligand scaffold as well as its ability to participate in redox reaction by being redox-non-innocent, which results in the facile multi-electron-transfer

process via metal—ligand cooperation during oxidation processes. Kinetic analysis suggests involvement of a single Ru-complex in catalysis where O—O bond formation most likely proceeds via radical coupling between the oxygen atom of ruthenium-oxo species and the oxygen atom of Ce^{IV}—OH ion (I2M-HC pathway depicted in Scheme 1). This interpretation is further justified by density functional theory (DFT) calculations. The participation of Ce^{IV}—OH ion in O—O bond formation is an important observation from the viewpoint of natural oxygen evolution reaction in Mn_4CaO_5 cluster where the O—O bond formation was proposed to occur through the heterometallic reaction between Mn^V=O species and Ca^{II}—OH species.[20] Thus, the present work demonstrates the benefits of using a redox-active ligand for carrying out multielectron reactions and provides insights into catalytic water oxidation through a nonconventional pathway.

RESULTS AND DISCUSSION

Synthesis and Characterizations. The ruthenium(III) complex was synthesized by reacting ligand H_3L with triethylamine and *cis*-$[Ru(DMSO)_4(Cl)_2]$ (DMSO = dimethyl sulfoxide) in methanol under refluxing condition, followed by addition of excess 4-methylpyridine. After evaporation of solvent, the residue was dissolved in dichloromethane and layered with hexane. This afforded the isolation of the compound as green microcrystalline solid. Very few single crystals of X-ray diffraction quality were also obtained by this method. The structural analysis reveals that complex is cocrystallized with free H_3L ligand and dichloromethane (**1-Ru^{III}·H$_3$L·CH$_2$Cl$_2$**), where the free H_3L ligand is involved in H-bonding interaction with ruthenium complex as shown in Figure S1. The ORTEP view of the molecular structure of complex **1-Ru^{III}** is presented in Figure 1. The selected bond
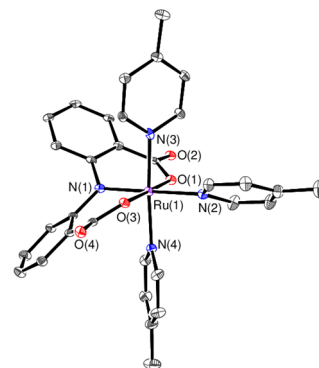

Figure 1. ORTEP (30%) view of the metal coordination environment in the crystal of $[Ru(L)(pic)_3]·H_3L·CH_2Cl_2$ (**1-Ru^{III}·H$_3$L·CH$_2$Cl$_2$**). Carbon atoms are not labeled. Hydrogen atoms are omitted for clarity. The free H_3L ligand and CH$_2$Cl$_2$ are not shown for clarity.

lengths and bond angles are displayed in Table 1. The crystal structure shows that the Ru^{III} center adopts a distorted octahedral geometry. The tridentate L^{3-} ligand occupies the equatorial plane in a meridional fashion. The fourth position in the equatorial plane and the two axial positions are occupied by the nitrogen atom from 4-methylpyridine ligands. The two phenyl rings of L^{3-} ligand do not remain in one plane. The dihedral angle between them is determined to be 63.118(11)°. The Ru—N(4-methylpyridine) bond at the equatorial position [Ru(1)—N(2) = 2.127 Å] is found to be relatively longer compared to the Ru(1)—N(1) bond distance (1.940 Å), as

Table 1. Selected Bond Lengths (Å) and Bond Angles (deg) of the Metal Coordination Environment in the Crystal of 1-Ru^{III}·H$_3$L·CH$_2$Cl$_2$

Ru(1)−N(1)	1.940(3)	Ru(1)−N(4)	2.103(3)
Ru(1)−N(2)	2.127(3)	Ru(1)−O(1)	2.054(2)
Ru(1)−N(3)	2.093(3)	Ru(1)−O(3)	2.039(2)
N(1)−Ru(1)−N(2)	178.04(11)	N(2)−Ru(1)−O(1)	92.37(10)
N(1)−Ru(1)−N(3)	93.02(12)	N(2)−Ru(1)−O(3)	88.66(10)
N(1)−Ru(1)−N(4)	91.18(12)	N(3)−Ru(1)−O(1)	89.84(10)
N(2)−Ru(1)−N(3)	86.04(11)	N(3)−Ru(1)−O(3)	89.63(10)
N(2)−Ru(1)−N(4)	89.77(12)	N(4)−Ru(1)−O(1)	90.41(10)
N(3)−Ru(1)−N(4)	175.80(11)	N(4)−Ru(1)−O(3)	90.19(10)
N(1)−Ru(1)−O(1)	89.35(11)	O(1)−Ru(1)−O(3)	178.81(9)
N(1)−Ru(1)−O(3)	89.61(10)		

observed for other reported Ru-complexes.[14] This phenomenon might be attributed as trans-labilizing effect of the N(1) atom of L^{3-} ligand. The two axial Ru−N(4-methylpyridine) bonds [Ru(1)−N(3) = 2.093 Å; Ru(1)−N(4) = 2.103 Å] are relatively shorter than that at the equatorial position, so it might be presumed that due to trans-labilizing effect the 4-methylpyridine group at equatorial position is vulnerable to exchange with water during catalytic water oxidation reaction (see below).

The presence of free H$_3$L ligand in the compound might interfere with the physicochemical properties of the ruthenium(III) complex; therefore, isolated **1-Ru^{III}**·H$_3$L·CH$_2$Cl$_2$ product was further purified by flash chromatography over silica with CH$_3$OH/CH$_2$Cl$_2$ (1:9, v/v) as eluents. Despite our effort, we failed to grow single crystals of the purified complex. We believe that the H-bonding interaction of the free ligand with ruthenium complex is necessary for proper crystal packing of the molecule. The purified complex has been characterized by elemental analysis and various spectroscopic techniques, viz., mass spectroscopy, ^{1}H NMR, EPR, and UV−vis. Elemental analysis reveals the composition of the complex as **1-Ru^{III}**·CH$_3$OH·2H$_2$O. The HRMS spectrum of the compound in methanol shows an intense peak at m/z = 636.1324, attributed to [**1-Ru^{III}** + H]$^+$, which confirms the mononuclear structure of the complex (Figure S2). The ^{1}H NMR spectrum of the complex in CD$_3$OD/acidic-D$_2$O (4:1, v/v) after reducing with Na$_2$S$_2$O$_4$ shows 20 proton resonances in the aromatic region (Figure S3). The methyl protons of the equatorial and axial 4-methylpyridine ligands resonate in a ratio of 1:2 at δ = 2.20 ppm and δ = 2.64 ppm, respectively. Thus, the shielding effect on the equatorial 4-methylpyridine ligand is greater than that of the two axial ones. This can be explained by considering the strong σ-donating as well as the weak π-accepting property of the nitrogen atom of the tridentate ligand, favoring the back-donating effect of the ruthenium(II) core in the trans position. This would affect the equatorial 4-methylpyridine group directly by inducing more electron density on it, resulting in more shielding effect on the equatorial ligand compared to that on the axial ones. The X-band EPR spectrum of **1-Ru^{III}**, recorded at 77 K in anhydrous methanol, shows responses typical for low spin d^5 Ru^{III} species with axial g component splitting at $g_{x,y}$ = 2.19 and g_z = 1.90 (Figure S4).[21] The UV−vis spectrum[14a] of **1-Ru^{III}** in anhydrous methanol is shown in Figure S5. The compound shows two intense absorption bands in the near-UV region at λ = 308 and 336 nm, tentatively assigned as the ligand(pπ) → ligand(pπ*) electronic transition. Two more long-wavelength

absorption bands at λ = 508 and 690 nm are observed. These transitions can be assigned as ligand-to-metal charge transfer (LMCT).[22]

Ligand Exchange and Generation of Aqua Coordinated Species. In order for Ru-WOCs to participate in the water oxidation reaction, it is necessary for them to have access to the corresponding aqua complex. The displacement of 4-methylpyridine with water would allow to access the catalytically important "Ru−OH$_2$" species. This phenomenon was observed previously for other reported Ru-WOCs.[8,12−14] The aqua-ligation enables the PCET process, which facilitates the generation of catalytically active high-valent ruthenium-oxo intermediates at a much lower potential. The possible 4-methylpyridine−water exchange event with complex **1-Ru^{III}** was examined by HRMS and ^{1}H NMR studies in aqueous media. HRMS analysis of **1-Ru^{III}** in an acidic-water/methanol (4:1, v/v) mixture resulted in the appearance of signal at m/z = 544.0811 corresponding to {[Ru(L)(pic)$_3$] − pic + 2H$^+$ + e$^-$}$^{1+}$; however, no signal for {[Ru(L)(pic)$_3$] + H}$^{1+}$ (m/z = 636.1324) was observed under aqueous condition (Figure S6). This result points to the fact that under aqueous condition one of the 4-methylpyridine ligands is prone to be displaced from **1-Ru^{III}** and thus creates a free coordination site for an aqua ligand. In fact, signals for free 4-methylpyridine protons were observed in ^{1}H NMR of **1-Ru^{III}** recorded in acidic-D$_2$O/CD$_3$OD (4:1, v/v) solvent mixture (Figure S7). Moreover, the absorption bands observed at 508 and 690 nm due to [Ru(L)(pic)$_3$] (**1-Ru^{III}**) in anhydrous methanol were red-shifted to 534 and 703 nm, respectively, in acidic (pH 1) aqueous solution (Figure S8). This observation can be realized due to the coordination of water by replacing one of the 4-methylpyridine ligands in complex **1-Ru^{III}**. This proposition is also manifested in EPR spectrum of **1-Ru^{III}** when recorded in two different solvents, methanol and water. In methanol, **1-Ru^{III}** shows an axial EPR spectrum (Figure S4) with $g_{x,y}$ = 2.19, g_z = 1.90, while in aqueous solution a rhombic spectrum with g-tensors at g_x = 2.21, g_y = 2.14, g_z = 1.91 is obtained (Figure S9). This observed rhombic nature ($g_x \neq g_y \neq g_z$) implies that a rearrangement in the ligand sphere of **1-Ru^{III}** occurs in aqueous media.[23] The replacement of one of the 4-methylpyridine ligand by water would introduce more asymmetry in the coordination sphere of Ru ion (N−N, N−O, and O−O donor atoms in three coordinates) compared with **1-Ru^{III}** (two N−N and one O−O donor atoms in three coordinates), which may be considered to originate larger rhombicity in aqueous media. Thus, on the basis of the above results we believe that the ligand interchange occurs most likely at the Ru^{III} state. The ligand displacement reaction could in principle occur at two positions, in either the equatorial or axial position as shown in Figure 2. Considering the trans-labilizing effect of the nitrogen atom of L^{3-} ligand, as found in
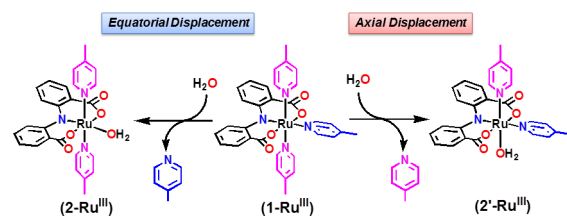
Figure 2. Ligand-exchange pathways leading to the formation of two isomeric aqua-coordinated complexes **2-Ru^{III}** and **2′-Ru^{III}**.

the crystal structure of **1-Ru^{III}**, the equatorial position would be susceptible for 4-methylpyridine−water ligand exchange. For further support, DFT calculations (see the Supporting Information) were performed to determine the relative energies of two isomeric ruthenium(III)-aqua complexes at a doublet ground state including solvation. Complex **2-Ru^{III}** with H$_2$O coordinated at the equatorial position is found to be 5.84 kcal/mol more stable than complex **2′-Ru^{III}** where H$_2$O was coordinated at the axial position. Therefore, equatorial isomer **2-Ru^{III}** is presumed to act as a true catalyst; hereafter, we consider only the equatorial structure of various other intermediates (see below) for further discussions.

Electrochemical Study. To get insight into the redox behavior of complex **1-Ru^{III}**, electrochemical measurements by means of cyclic voltammogram (CV) and square wave voltammogram (SWV) were carried out in both organic solvent as well as in aqueous media. All redox potentials reported here are versus NHE. In anhydrous acetonitrile complex **1-Ru^{III}** shows only one redox response at $E_{1/2}$ = 0.73 V (ΔE = 90 mV, i_{pa}/i_{pc} = 1.66) attributed to [Ru^{IV}(L)(pic)$_3$]$^+$/[Ru^{III}(L)(pic)$_3$] couple (Figure S10). However, in aqueous media various redox responses from the in situ generated ruthenium(III)-aqua species, [Ru(L)(pic)$_2$(OH$_2$)] (**2-Ru^{III}**), are observed (*vide supra*). The CV and SWV curves of **2-Ru^{III}** in CF$_3$SO$_3$H (pH ∼1.25) aqueous solution containing 25% CF$_3$CH$_2$OH are shown in Figure 3. The CV curve of **2-Ru^{III}**

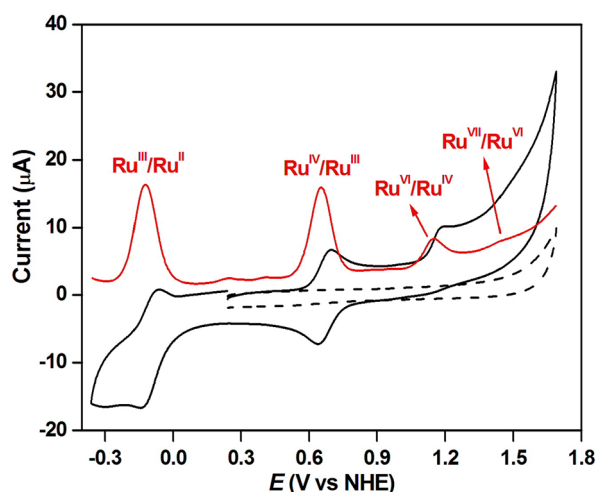**Figure 3.** CV (black line) and SWV (red line) of complex **2-Ru^{III}** at pH 1.25 in CF$_3$SO$_3$H aqueous solution containing 25% CF$_3$CH$_2$OH. Black dashed line represents blank CV. Conditions: [**2-Ru^{III}**] = 1 mM, scan rate of CV = 0.1 V·s^{-1}, for SWV frequency = 15 Hz, amplitude = 0.025 V, working electrode: glassy carbon.

shows one reduction wave and three oxidation waves along with a larger electro-catalytic wave at an onset potential of ∼1.40 V. This catalytic wave is associated with electrochemical oxidation of water. The SWV curve exhibits four redox peaks at the potentials of −0.13, 0.66, 1.15, and 1.46 V. The first redox event at the potential of −0.13 V is tentatively assigned as Ru^{III}/Ru^{II} redox couple. Because of the presence of negatively charged ligand, the Ru^{III}/Ru^{II} redox couple appears at a markedly lower potential than those of WOCs containing neutral[10,16,17] as well as anionic donor ligands,[13,14] which implies a much enhanced donor ability of the anionic L^{3-} ligand. In order to know the number of electron transfers involved in the second and third redox events, controlled

potential electrolysis (CPE) experiments were carried out at 0.80 and 1.25 V, respectively, at pH ∼1. The CPE analyses confirm the one-electron nature of the second redox event and the two-electron nature of the third redox event (Figure S11). The bulk solutions after electrolyses at 0.80 and 1.25 V were examined by CV scans. As shown in Figure S12, similar redox features were obtained before and after CPE analyses. These findings imply that the complex mostly retains its mononuclear structure even at the higher oxidation states (*vide infra*), unlike the event for [Ru(pdc)(py)$_3$] (H$_2$pdc = 2,6-pyridinedicarboxylic acid, py = pyridine) complex where dimerization was demonstrated during the oxidation process.[24] Therefore, on the basis of CPE analysis the four redox signals observed at −0.13, 0.66, 1.15, and 1.46 V in SWV can formally be assigned as Ru^{III}/Ru^{II}, Ru^{IV}/Ru^{III}, Ru^{VI}/Ru^{IV}, and Ru^{VII}/Ru^{VI} redox couple, respectively (see the Pourbaix diagram in Figure 4). The Ru^{VII}/Ru^{VI} redox potential lies on the onset of the catalytic wave, implying the formal high-valent Ru^{VII} species is responsible for triggering the oxidation of water.
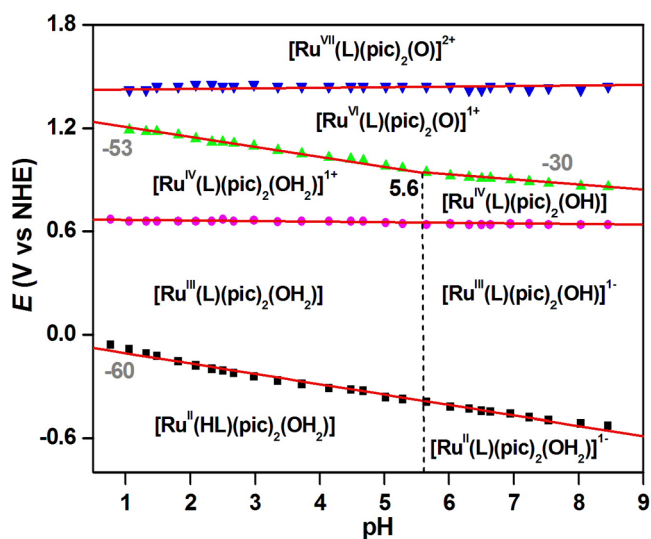

Figure 4. Pourbaix diagram of **2-Ru^{III}** in Britton−Robinson buffer aqueous solution containing 25% CF$_3$CH$_2$OH. pK_a value is denoted by the vertical dashed line.

To get further insights about the PCET processes and various redox compositions generated during oxidation, electrochemistry analysis of complex **2-Ru^{III}** was conducted over the pH range from 0.77 to 8.45. The redox potentials were determined by means of SWV (Figure S13) and represented in Figure 4. The Pourbaix diagram analysis indicates that at a Ru^{II} state the tridentate ligand (L) exists in two different protonated forms giving rise to species [Ru^{II}(HL)(pic)$_2$(OH$_2$)] (**2-Ru^{II}**) and [Ru^{II}(L)(pic)$_2$(OH$_2$)]$^{1-}$. The first Ru^{III}/Ru^{II} redox potential varies linearly with pH over the entire pH range with a slope of −60 mV/pH, which implies a one-electron and one-proton (1e$^-$, 1H$^+$) PCET process. Therefore, we assign the redox couple in the region 0.77 < pH < 5.6 to [Ru^{III}(L)(pic)$_2$(OH$_2$)]/[Ru^{II}(HL)(pic)$_2$(OH$_2$)], whereas the redox couple ranging 5.6 < pH < 8.45 to [Ru^{III}(L)(pic)$_2$(OH)]$^{1-}$/[Ru^{II}(L)-(pic)$_2$(OH$_2$)]$^{1-}$. The second Ru^{IV}/Ru^{III} redox process is pH-independent within whole pH window, indicating that only an electron-transfer process is involved. Therefore, the redox processes at pH below and above 5.6 correspond to the formal

Table 2. Experimental and Calculated Redox Potentials of 2-Ru^{III} at pH 1.25 vs NHE

elemental steps	$E^{expt\,a}$	$E^{DFT\,b}$	
		BP86	B3LYP
$[Ru^{III}(L)(pic)_2(OH_2)] + 1e^- + 1H^+ \rightarrow [Ru^{II}(HL)(pic)_2(OH_2)]$ (2-Ru^{III}) (2-Ru^{II})	−0.13	−0.49	−0.52
$[Ru^{IV}(L)(pic)_2(OH_2)]^{1+} + 1e^- \rightarrow [Ru^{III}(L)(pic)_2(OH_2)]$ (2-Ru^{IV}) (2-Ru^{III})	0.66	0.54	0.54
$[Ru^{VI}(L)(pic)_2(O)]^{1+} + 2e^- + 2H^+ \rightarrow [Ru^{IV}(L)(pic)_2(OH_2)]^{1+}$ (2-Ru^{VI}) (2-Ru^{IV})	1.15	1.11	1.21
$[Ru^{VII}(L)(pic)_2(O)]^{2+} + 1e^- \rightarrow [Ru^{VI}(L)(pic)_2(O)]^{1+}$ (2-Ru^{VII}) (2-Ru^{VI})	1.46	1.76	1.85

^{a}Experimental potentials were obtained from SWV in pH 1.25 aqueous CF$_3$SO$_3$H acid solution containing 25% CF$_3$CH$_2$OH. ^{b}Redox potentials were calculated using methods BP86/def2-TZVPP/COSMO and B3LYP/def2-TZVP/COSMO (for further details, see the Supporting Information).

$[Ru^{IV}(L)(pic)_2(OH_2)]^{1+}/[Ru^{III}(L)(pic)_2(OH_2)]$ and $[Ru^{IV}(L)(pic)_2(OH)]/[Ru^{III}(L)(pic)_2(OH)]^{1-}$ redox couples, respectively. The third redox event comprises two different PCET processes depending on pH. At 0.77 < pH < 5.6, the oxidation potential decreases linearly with a slope of −53 mV/pH. The CPE analysis revealed that two-electron oxidation occurred at this stage as stated above, so this phenomenon can be attributed to an oxidation from formal $[Ru^{IV}(L)(pic)_2(OH_2)]^{1+}$ (2-Ru^{IV}) to $[Ru^{VI}(L)(pic)_2(O)]^{1+}$ (2-Ru^{VI}), a (2e$^-$, 2H$^+$) PCET process which is apparently equivalent to a (1e$^-$, 1H$^+$) process. In contrast, in pH region 5.6 < pH < 8.45, the oxidation potential decreases linearly with a slope of −30 mV/pH, corresponding to formation of formal $[Ru^{VI}(L)(pic)_2(O)]^{1+}$ (2-Ru^{VI}) species by a (2e$^-$, 1H$^+$) PCET process from $[Ru^{IV}(L)(pic)_2(OH)]$. The fourth and last oxidation process occurs at relatively constant potential of 1.46 V vs NHE over entire pH window. This can be regarded as only electron transfer to generate formal $[Ru^{VII}(L)(pic)_2(O)]^{2+}$ (2-Ru^{VII}) species which triggers water oxidation. This is a rare example of Ru-based WOC where water oxidation proceeds via a formal Ru^{VII} state.[12a] Therefore, on the basis of the Pourbaix diagram the four redox elemental steps occurring at acidic pH can be summarized as given in Table 2. Furthermore, the redox potentials were calculated by DFT to support these assignments (Table 2). The deviations found between experimental and calculated values are within the error expected for DFT calculations.

Redox Titration and Spectroscopic Characterization of Intermediates. The redox titration of complex 2-Ru^{III} was performed with ceric ammonium nitrate (CAN) in acidic media (pH 1 aqueous CF$_3$SO$_3$H acid solution containing 25% CF$_3$CH$_2$OH) in order to detect the intermediates formed upon oxidation. The titration was followed by UV−vis spectroscopy monitoring the change of absorbance at 365 nm band as depicted in Figure S14a. The spectra of complex 2-Ru^{III} at different oxidation states are shown in Figure 5. Upon addition of 1 equiv of CAN to complex 2-Ru^{III}, a distinct color change from green to red was observed. In UV−vis spectra, with incremental addition of CAN up to 1 equiv, the intensities of $\pi \rightarrow \pi^*$ band at 330 nm and LMCT band at 703 nm decrease steadily, while a band at 511 nm develops prominently (Figure S14b). As evident from the titration curve shown in Figure S14a, this variation in spectral features is related with formation of a one-electron-oxidized formal Ru^{IV} species, 2-Ru^{IV}. Two isosbestic points at λ = 430 and 587 nm are observed during transformation of 2-Ru^{III} to 2-Ru^{IV}. The
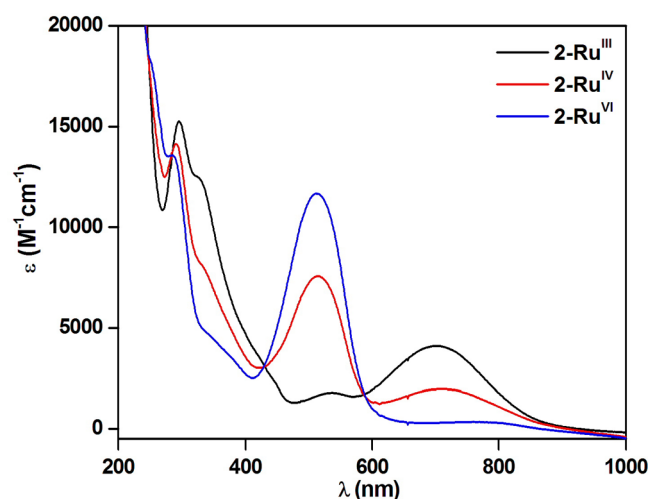

Figure 5. UV−vis spectra of 2-Ru^{III} at different oxidation states generated from stoichiometric oxidation with Ce^{IV} in pH ~1 aqueous CF$_3$SO$_3$H solution containing 25% CF$_3$CH$_2$OH.

appearance of isosbestic points implies a clean transformation of 2-Ru^{III} → 2-Ru^{IV}. Addition of 2 equiv more of CAN to 2-Ru^{IV} caused further lowering in intensity of 330 nm band with increasing in intensity of 511 nm band (Figure S14c). The LMCT band at 703 nm becomes almost featureless at this stage. This might be correlated with the generation of formal Ru^{VI} intermediate (2-Ru^{VI}), as evident from isosbestic points at λ = 428 and 590 nm and titration curve. No considerable changes were observed after further addition of CAN, probably due to its rapid consumption for oxidation of water. Thus from redox titration it is obvious that complex 2-Ru^{III} undergoes one- and two-electron oxidation successively to generate formal Ru^{IV} and Ru^{VI} intermediates, respectively. These observations corroborate well with the electrochemical behavior of 2-Ru^{III} described above. Furthermore, the UV−vis spectral features of Ru^{IV} and Ru^{VI} species generated by bulk electrolysis at 0.80 and 1.25 V vs NHE, respectively (Figure S15), resemble those obtained in CAN titration, implying the formation of the same oxidized species electrochemically or chemically.

HRMS-ESI spectroscopy was further employed to detect the oxidized species. Addition of 1 equiv of CAN to an acidic-water/methanol (4:1, v/v) solution of 2-Ru^{III} produces a major signal at m/z = 544.0811, which corresponds to a $\{[Ru^{II}(HL)(pic)_2] + H^+\}^{1+}$ ion, implying that 2-Ru^{IV} under-

goes facile reduction with the loss of aqua ligand under ESI-MS condition (Figure S16), while upon addition of an excess 10 equiv of CAN, a new signal at m/z = 608.1022 appeared along with the signal for $\{[Ru^{II}(HL)(pic)_2] + H^+\}^{1+}$ ion (Figure S17). The new signal at m/z = 608.1022 can be attributed to a $\{[Ru^{VI}(L)(pic)_2(O)]^+ + CH_3OH + H_2O\}^{1+}$ ion, suggesting the formation of a formal ruthenium(VI)-oxo intermediate. The CH_3OH and H_2O might have been involved in a hydrogen-bonding interaction with ruthenium(VI)-oxo species producing an ion together. We note here that no signals related to Ru-dimers are observed, discarding the possibility of formation of dimer under our experimental condition or time scale.

Computational Studies: Electronic Description of Various Redox Intermediates. The ligand L^{3-}, being redox-non-innocent in nature, would participate in redox reactions as shown in Scheme 3. Hence, metal−ligand

Scheme 3. Redox Processes Involved in Ligand L^{3-}
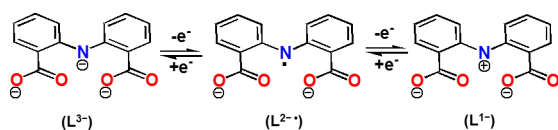
cooperation is expected in the electron-transfer process to generate various oxidized intermediates from **2-Ru^{III}**. DFT calculations (see the Supporting Information) were performed to get insight into the electronic structures of the various redox intermediates, viz., **2-Ru^{IV}**, **2-Ru^{VI}**, and **2-Ru^{VII}** generated during oxidation of **2-Ru^{III}** in acidic media. The optimized structures are displayed in Figure 6, and the results are summarized in Table 3. The spin density plots are depicted in Figure S18.
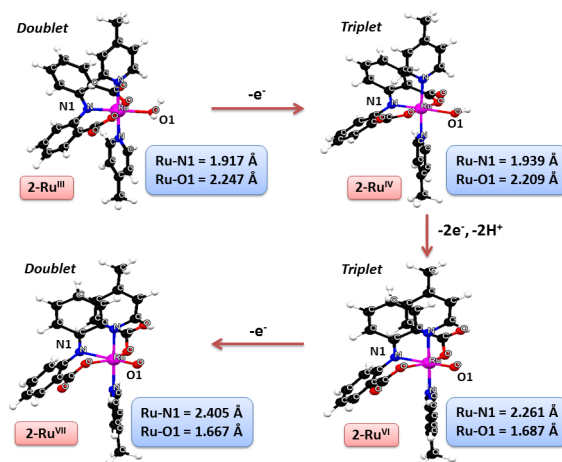
Figure 6. Optimized structures at B3LYP/def2-TZVP level of theory of the various redox intermediates formed during oxidation of **2-Ru^{III}** in acidic media.

The structure of complex **2-Ru^{III}** was initially optimized in the doublet state. The spin density on the Ru center was calculated to be 0.65 and the remaining spin density was delocalized on the tridentate ligand framework (0.35). Thus, the oxidation state of Ru center can be assigned as +III. This was further verified by EPR spectroscopy as shown in Figure S9.[23] One-electron oxidation of **2-Ru^{III}** generates the formal

Table 3. Relative Energies (kcal/mol) of Different Spin States and Spin Densities on Selected Atoms and Ligand Scaffold[a]

formal redox state (species)	spin state	relative energy (kcal/mol)	spin density		
			Ru	O[b]	L[c]
Ru^{III} (**2-Ru^{III}**)	doublet	0.00	0.65		0.35
Ru^{IV} (**2-Ru^{IV}**)	singlet[d]	2.41	−0.56	0.00	0.56
	triplet	0.00	1.09	0.00	0.90
Ru^{VI} (**2-Ru^{VI}**)	singlet[d]	13.32	−0.34	−0.71	1.06
	triplet	0.00	0.53	0.46	0.99
	quintet	12.63	1.76	0.91	1.32
Ru^{VII} (**2-Ru^{VII}**)	doublet	0.00	0.51	0.47	0.00
	quartet	13.53	1.60	0.93	0.47
	sextet	29.36	1.73	0.96	2.26

[a]Calculations were performed at the B3LYP/def2-TZVP level of theory. Spin densities were estimated using Mulliken population analysis. [b]O represents the oxygen atom of aqua/oxo ligand. [c]L represents the tridentate ligand. [d]Calculated using broken-symmetry formalism.

Ru^{IV} species, labeled as **2-Ru^{IV}**. The ground state of **2-Ru^{IV}** was found to be triplet, and the singlet state (calculated with broken-symmetry formalism) was 2.41 kcal/mol higher in energy than the triplet state. The spin densities on Ru and ligand framework (L) at triplet state were determined to be 1.09 and 0.90, respectively. Therefore, the formal Ru^{IV} complex (**2-Ru^{IV}**) can be better described as featuring low-spin Ru^{III} center with significant radical character on the ligand backbone, where the two unpaired spins are ferromagnetically coupled, giving rise to a $S = 1$ system. Thus, complex **2-Ru^{IV}** can be represented as $[Ru^{III}(L^{2-•})(pic)_2(H_2O)]^{1+}$ where a ligand-centered oxidation is predicted. Subsequent ($2e^-$, $2H^+$) oxidation of **2-Ru^{IV}** generates the formal Ru^{VI}=O intermediate (labeled as **2-Ru^{VI}**). In **2-Ru^{VI}**, the triplet state ($S = 1$) was found to be the ground state. On the basis of spin densities (0.53 on Ru, 0.46 on O, 0.99 on L), the electronic structure of **2-Ru^{VI}** can be best described as $[Ru^{V}(L^{2-•})(pic)_2(=O)]^{1+}$ featuring a low-spin Ru^{V} ($S = 1/2$) ferromagnetically coupled with ligand radical ($S = 1/2$). The spin on Ru^{V} was found to be delocalized over the oxo group. The related singlet (broken-symmetry) and quintet states were found to be 13.32 and 12.63 kcal/mol higher in energy, respectively. The calculated structure of **2-Ru^{VI}** at the triplet state features short Ru−O (1.687 Å) and elongated Ru−N (2.261 Å) bonds. The triplet ground states ($S = 1$) of both **2-Ru^{IV}** and **2-Ru^{VI}** were proven by EPR spectroscopy (Figure S19). Both the oxidized species show an intense broad signal between 200 and 400 mT along with a weak half-field EPR line at 158 mT. This half-field signal is typical for a $S = 1$ spin state and corresponds to $\Delta M_S = 2$ forbidden transition.[25] Finally, one-electron oxidation of **2-Ru^{VI}** furnishes the formal high-valent Ru^{VII}=O intermediate, **2-Ru^{VII}**. In **2-Ru^{VII}**, the doublet state was shown to be ground state, whereas the quartet and sextet states were 13.53 and 29.36 kcal/mol higher in energy, respectively. In the doublet ground state, no unpaired spin density was found on the ligand frame, indicating that oxidation happened at ligand center. Thus, the doublet state of **2-Ru^{VII}** can be represented as $[Ru^{V}(L^{1-})(pic)_2(=O)]^{2+}$ with a low-spin Ru^{V} ($S = 1/2$) center. A very elongated Ru−N bond (2.405 Å) was estimated from the calculated structure of **2-Ru^{VII}**, which signifies the poor donor ability of the positively charged N-atom.

Substantial spin density (47%) was found to be located on the O(oxo) atom. Therefore, the Ru-oxo moiety of the $[Ru^V(L^{1-})(pic)_2(=O)]^{2+}$ species (**2-Ru^{VII}**) can exhibit a metal-oxyl mode of reactivity by virtue of the nascent radical character on O(oxo) atom (see below). Thus, it is evident that the non-innocent ligand plays an important role in the electron-transfer process by storing redox equivalents, thereby relieving the metal center from being heavily oxidized.

Chemical Water Oxidation. The catalytic water oxidation mediated by **1-Ru^{III}** was examined using CAN as the sacrificial oxidant in acidic aqueous solution (pH ~1). As stated above, in aqueous solution **1-Ru^{III}** readily undergoes ligand−water exchange to generate a water-coordinated complex, **2-Ru^{III}**. Therefore, for catalysis study a solution of complex **2-Ru^{III}** of desired concentration was prepared by dissolving **1-Ru^{III}** in pH 1 aqueous CF_3SO_3H solution containing 25% CF_3CH_2OH, assuming 100% conversion. The evolution of dioxygen was monitored using differential pressure manometer and authenticated by GC analysis at the end of the measurement. Upon addition of an excess amount of CAN (100 mM) to the complex solution (10 μM), rapid evolution of dioxygen gas was observed. After 1 h, the oxygen evolution reached a plateau, producing turnover numbers of 200. The initial rate of oxygen evolution was found to be proportional to the concentration of catalyst **2-Ru^{III}**, following a pseudo-first-order reaction with a first-order rate constant of 0.168 s^{-1} (Figure 7). This first-order
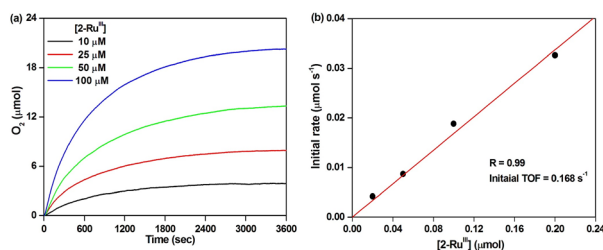
Figure 7. (a) Oxygen evolution profiles at various concentrations of catalyst **2-Ru^{III}** in pH 1 CF_3SO_3H solution and CF_3CH_2OH mixture (3:1) (total volume 2 mL) containing CAN (100 mM) at 25 °C. (b) Initial rate of O_2 production at various concentrations of catalyst **2-Ru^{III}**.

rate constant which is equal to the turnover frequency (TOF) is remarkably higher than the TOFs of reported mononuclear Ru-WOCs having neutral polypyridyl ligands.[1,10,16,17] Although complex **2-Ru^{III}** catalyzes water oxidation rapidly with high TOF, the catalytic performance is limited to moderate turnovers. This suggests that the catalyst degrades in a side reaction under highly oxidizing condition. In order to identify the degraded or deactivated product, we performed a catalysis reaction at a 1 mM/100 mM [catalyst]/[CAN] ratio, and the postcatalysis reaction mixture was then analyzed by MALDI mass spectroscopy (Figure S20). The spectrum shows a signal at m/z = 571, assigned to a species $\{[Ru^{II}(HL)(4\text{-}HCO\text{-}py)_2] + H^+\}^{1+}$ (4-HCO-py = 4-pyridinecarboxaldehyde) where 4-methylpyridine ligand was found to be oxidized to 4-pyridinecarboxaldehyde. A similar type of ligand oxidation was also documented in the literature for a $[Ru(bda)(pic)_2]$ complex (H$_2$bda = 2,2′-bipyridine-6,6′-dicarboxylic acid, pic = 4-methylpyridine).[26] Therefore, oxidation of the auxiliary 4-methylpyridine ligand could be regarded as one of the possible deactivation process.

Kinetic Study and Mechanistic Interpretation. Kinetic analysis of the catalytic water oxidation reaction catalyzed by **2-Ru^{III}** was followed by monitoring the depletion of Ce^{IV} absorption band at 360 nm using UV−vis spectrophotometer (Figures S21 and S22). The initial rate method was used to analyze the kinetic data to avoid the effect of side reaction as described above. When the initial concentration of CAN was kept constant (2 mM) and catalyst concentration was varied (10−25 μM range), a linear dependency between CAN depletion and the concentration of **2-Ru^{III}** was observed. The pseudo-first-order rate constant was measured as k_{obs} = 0.68 s^{-1} (Figure 8a). The first-order dependence of rate with respect to catalyst confirms that single ruthenium complex is involved in catalytic water oxidation reaction.
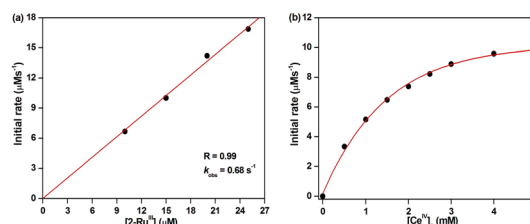
Figure 8. (a) Plot of initial rates of Ce^{IV} consumption versus [**2-Ru^{III}**] at 2 mM CAN. (b) Plot of initial rates versus [Ce^{IV}] for catalyst **2-Ru^{III}** (10 μM).

In contrast, the order of reaction with respect to CAN varied with concentration of CAN. At lower concentration (<1.5 mM) the reaction rates increased linearly with [CAN], whereas at higher concentration of CAN, saturation behavior was observed (Figure 8b). This observed kinetic profile could be modeled as Michaelis−Menten-like kinetics as shown in Scheme 4, where the highly oxidized $[Ru^V(L^{1-})(pic)_2(=O)]^{2+}$ (**2-Ru^{VII}**) reacts reversibly with **Ce^{IV}−OH** species to form intermediates before the rate determining step (k_2).

Scheme 4. Proposed O−O Bond Formation Pathway and Subsequent Formation of Various Intermediates Prior to Release of O_2[a]
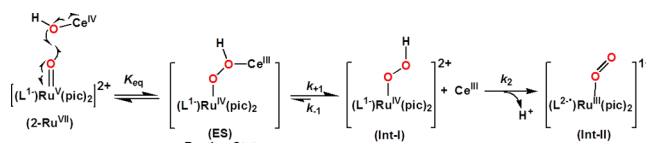
[a]pic = 4-methylpyridine; **Ce^{IV}−OH** = $[Ce^{IV}(OH)(NO_3)_5]^{2-}$ ion.

In a previous report, Sakai et al. revealed the singlet biradical character[15a] of a hydroxocerium(IV) moiety in hydrolyzed ceric species,[27] $[Ce^{IV}(OH)(NO_3)_5]^{2-}$ (labeled as **Ce^{IV}−OH**) where +0.89 and −1.02 of Mulliken spin densities were found at the O(hydroxide) and Ce atoms, respectively, so **Ce^{IV}−OH** ion can be better represented as $[Ce^{III}(^{\bullet}OH)(NO_3)_5]^{2-}$ where the O(hydroxide) atom possesses a highly radical-like character. Therefore, it is anticipated that the O−O bond formation event would most likely occur via radical−radical coupling between oxygen atoms of $[Ru^V(L^{1-})(pic)_2(=O)]^{2+}$ (**2-Ru^{VII}**) and **Ce^{IV}−OH** species (I2M−HC pathway as shown in Scheme 1), since the ruthenyl center also has substantial oxygen radicaloid character. It is noteworthy that the Ce^{IV} ion in this case acts not only as sacrificial oxidant but also plays an

important role in O−O bond formation event. The importance of the radical character of **Ce^{IV}−OH** ion in O−O bond formation was further supported by the fact that much lower oxygen evolution was observed when CAN was replaced with another powerful oxidant NaIO$_4$ (see Figure S23), which has redox potential of ~1.6 V vs NHE comparable with CAN's at pH 1.[28] The K_{eq} value describing the putative [Ru^{IV}(L^{1-})-(pic)$_2$-O-O(H)-Ce^{III}(NO$_3$)$_5$] (**ES**) adduct formation (Scheme 4) was determined to be 697 M^{-1}. The notably high K_{eq} value suggests that under catalytic condition virtually all catalysts should covert to **ES** adduct as the resting state. Successive decoordination of Ce(III) from **ES** adduct would generate a putative triplet Ru-hydroperoxo species [Ru^{IV}(L^{1-})-(pic)$_2$(OOH)]$^{2+}$ (**Int-I**); further removal of proton would result in the formation of putative quintet [Ru^{III}(L$^{2-\bullet}$)-(pic)$_2$(η^1-O$_2$)]$^{1+}$ species (**Int-II**) (Scheme 4, Figures 9 and S24, Table S2).
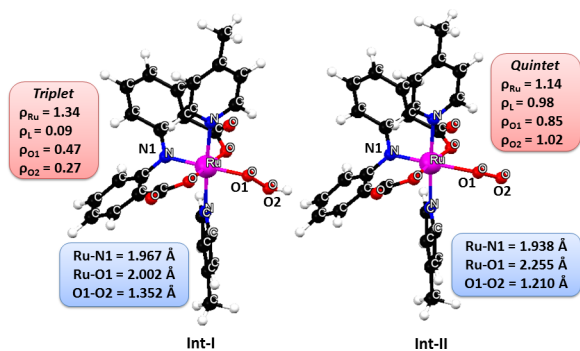

Figure 9. Optimized structures at B3LYP/def2-TZVP level of theory of intermediates **Int-I** and **Int-II**. Spin densities (ρ) are indicated for selected atoms. L represents the tridentate ligand.

To rationalize further the proposed elementary steps as shown in Scheme 4, reaction of **2-Ru^{VII}** with 1 equiv of CAN was followed by UV−vis spectrophotometer, and the spectral changes were analyzed by ReactLab Kinetics version 1.1. The global analysis affords the kinetic parameters as log K_{eq} = 2.79, k_{+1} = 4.02 × 10^2 s^{-1}, k_{-1} = 8.26 × 10^1 s^{-1}, and k_2 = 1.94 × 10^{-1} s^{-1}. The fitted time trace at 605 nm, calculated spectra for the various species, and the calculated time-dependent species distribution diagram are displayed in Figure S25. The rate constant value of k_2 is comparable with the catalytic turnover frequency (TOF) obtained from the amount of oxygen evolved in catalytic reaction, supporting our proposed model. Therefore, the cleavage of O−H bond to generate **Int-II** is likely to be the rate-determining step for the Ce(IV)-driven water oxidation catalyzed by **2-Ru^{III}**. In fact the H/D kinetic isotope effect (KIE) of 3.1 was determined from initial rate of Ce^{IV} consumption in H$_2$O(pH 1)/D$_2$O(pD 1.4), affirming our conclusion (Figure S26). The driving force of O−H bond cleavage and release of H$^+$ could be attributed to the presence of a higher oxidizing equivalent in the ligand frame with a high-valent ruthenium center. In the final step, intermediate **Int-II** would release O$_2$ to regenerate **2-Ru^{IV}**. In **Int-II** at the quintet ground state, the Mulliken atomic spin densities (Ru = 1.14, L = 0.98, O$_{proximal}$ = 0.85, O$_{distal}$ = 1.02) and the O−O bond distance (1.21 Å) suggest that a triplet oxygen molecule coordinates with Ru^{III} center. Therefore, the displacement of a O$_2$ molecule by water is believed to occur rapidly to regenerate **2-Ru^{IV}**, which re-enters the catalytic cycle. Therefore, on the

basis of the experimental as well as computational studies addressed above, the overall proposed catalytic cycle for water oxidation mediated by **1-Ru^{III}** can be summarized as drawn in Figure 10.
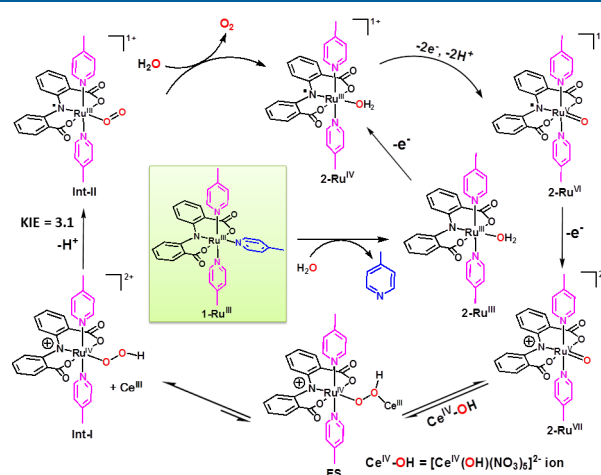

Figure 10. Overview of the proposed catalytic cycle of Ce^{IV}-driven water oxidation mediated by **1-Ru^{III}** in pH 1.

CONCLUSIONS

Herein, we report a mononuclear ruthenium(III) complex that effectively catalyzes water oxidation under pH 1/Ce^{IV} condition. The complex bears a negatively charged, redox-non-innocent tridentate ligand, which stabilizes the high-valent oxidation states of ruthenium. Experimental results along with computational studies support a mechanism where a formal high-valent Ru^{VII}=O species triggers the oxidation of water. Determination of the electronic structure by DFT calculations reveals that redox-active, anionic tridentate ligand actively participates in the electron-transfer process in cooperation with the metal ion. This metal−ligand cooperative effect facilitates accumulation of multiple oxidative equivalents at a single catalytic site which is required for a multielectron oxidation reaction such as water oxidation. Kinetic analysis reveals a nonconventional O−O bond formation pathway which largely relies on the radical character of the hydroxocerium(IV) species. Therefore, the results reported in this work demonstrate the benefit of using redox-non-innocent ligand in a designed catalyst and explore a nontraditional O−O bond formation pathway in water oxidation catalysis.

ASSOCIATED CONTENT

S **Supporting Information**

The Supporting Information is available free of charge at https://pubs.acs.org/doi/10.1021/acs.inorgchem.9b03258.

> Experimental details, computational methods, synthetic procedure, additional compound characterization data, experimental results, spin density plots, and geometry coordinates for optimized structures (PDF)

Accession Codes

CCDC 1936128 contains the supplementary crystallographic data for this paper. These data can be obtained free of charge via www.ccdc.cam.ac.uk/data_request/cif, or by emailing data_request@ccdc.cam.ac.uk, or by contacting The Cam-

bridge Crystallographic Data Centre, 12 Union Road, Cambridge CB2 1EZ, UK; fax: +44 1223 336033.

■ AUTHOR INFORMATION

Corresponding Authors
*E-mail: sukanta.mandal@chem.iitkgp.ac.in (S.M.).
*E-mail: anoop@chem.iitkgp.ac.in (A.A.).

ORCID ●
Anakuthil Anoop: 0000-0002-8116-5506
Sukanta Mandal: 0000-0001-6456-3898

Author Contributions
‖A.K., S.K.D., and S.D. contributed equally to this work.

Notes
The authors declare no competing financial interest.

■ REFERENCES

(1) Kärkäs, M. D.; Verho, O.; Johnston, E. V.; Åkermark, B. Artificial Photosynthesis: Molecular Systems for Catalytic Water Oxidation. *Chem. Rev.* **2014**, *114*, 11863−12001.

(2) Concepcion, J. J.; House, R. L.; Papanikolas, J. M.; Meyer, T. J. Chemical Approaches to Artificial Photosynthesis. *Proc. Natl. Acad. Sci. U. S. A.* **2012**, *109*, 15560−15564.

(3) Matheu, R.; Garrido-Barros, P.; Gil-Sepulcre, M.; Ertem, M. Z.; Sala, X.; Gimbert-Suriñach, C.; Llobet, A. The Development of Molecular Water Oxidation Catalysts. *Nat. Rev. Chem.* **2019**, *3*, 331−341.

(4) Berardi, S.; Drouet, S.; Francàs, L.; Gimbert-Suriñach, C.; Guttentag, M.; Richmond, C.; Stoll, T.; Llobet, A. Molecular Artificial Photosynthesis. *Chem. Soc. Rev.* **2014**, *43*, 7501−7519.

(5) Sala, X.; Maji, S.; Bofill, R.; García-Antón, J.; Escriche, L.; Llobet, A. Molecular Water Oxidation Mechanisms Followed by Transition Metals: State of the Art. *Acc. Chem. Res.* **2014**, *47*, 504−516.

(6) Kärkäs, M. D.; Åkermark, B. Water Oxidation Using Earth-Abundant Transition Metal Catalysts: Opportunities and Challenges. *Dalton Trans* **2016**, *45*, 14421−14461.

(7) (a) Neudeck, S.; Maji, S.; López, I.; Meyer, S.; Meyer, F.; Llobet, A. New Powerful and Oxidatively Rugged Dinuclear Ru Water Oxidation Catalyst: Control of Mechanistic Pathways by Tailored Ligand Design. *J. Am. Chem. Soc.* **2014**, *136*, 24−27. (b) Deng, Z.; Tseng, H.-W.; Zong, R.; Wang, D.; Thummel, R. Preparation and Study of a Family of Dinuclear Ru(II) Complexes That Catalyze the Decomposition of Water. *Inorg. Chem.* **2008**, *47*, 1835−1848. (c) Xu, Y.; Fischer, A.; Duan, L.; Tong, L.; Gabrielsson, E.; Åkermark, B.; Sun, L. Chemical and Light-Driven Oxidation of Water Catalyzed by an Efficient Dinuclear Ruthenium Complex. *Angew. Chem., Int. Ed.* **2010**, *49*, 8934−8937.

(8) Shatskiy, A.; Lomoth, R.; Abdel-Magied, A. F.; Rabten, W.; Laine, T. M.; Chen, H.; Sun, J.; Andersson, P. G.; Karkas, M. D.; Johnston, E. V.; Akermark, B. Catalyst-Solvent Interactions in a Dinuclear Ru-Based Water Oxidation Catalyst. *Dalton Trans* **2016**, *45*, 19024−19033.

(9) (a) Laine, T. M.; Kärkäs, M. D.; Liao, R.-Z.; Siegbahn, P. E. M.; Åkermark, B. A Dinuclear Ruthenium-Based Water Oxidation Catalyst: Use of Non-Innocent Ligand Frameworks for Promoting Multi-Electron Reactions. *Chem. - Eur. J.* **2015**, *21*, 10039−10048. (b) Wada, T.; Tsuge, K.; Tanaka, K. Synthesis and Redox Properties of Bis(hydroxoruthenium) Complexes with Quinone and Bipyridine Ligands. Water-Oxidation Catalysis. *Inorg. Chem.* **2001**, *40*, 329−337.

(10) Tong, L.; Thummel, R. P. Mononuclear Ruthenium Polypyridine Complexes That Catalyze Water Oxidation. *Chem. Sci.* **2016**, *7*, 6591−6603.

(11) (a) Duan, L.; Bozoglian, F.; Mandal, S.; Stewart, B.; Privalov, T.; Llobet, A.; Sun, L. A Molecular Ruthenium Catalyst with Water-Oxidation Activity Comparable to That of Photosystem II. *Nat. Chem.* **2012**, *4*, 418. (b) Fan, T.; Duan, L.; Huang, P.; Chen, H.; Daniel, Q.; Ahlquist, M. S. G.; Sun, L. The Ru-tpc Water Oxidation Catalyst and Beyond: Water Nucleophilic Attack Pathway versus Radical Coupling Pathway. *ACS Catal.* **2017**, *7*, 2956−2966. (c) Matheu, R.; Ertem, M. Z.; Benet-Buchholz, J.; Coronado, E.; Batista, V. S.; Sala, X.; Llobet, A. Intramolecular Proton Transfer Boosts Water Oxidation Catalyzed by a Ru Complex. *J. Am. Chem. Soc.* **2015**, *137*, 10786−10795.

(12) (a) Kärkäs, M. D.; Li, Y.-Y.; Siegbahn, P. E. M.; Liao, R.-Z.; Åkermark, B. Metal−Ligand Cooperation in Single-Site Ruthenium Water Oxidation Catalysts: A Combined Experimental and Quantum Chemical Approach. *Inorg. Chem.* **2018**, *57*, 10881−10895. (b) Karkas, M. D.; Liao, R.-Z.; Laine, T. M.; Akermark, T.; Ghanem, S.; Siegbahn, P. E. M.; Akermark, B. Molecular Ruthenium Water Oxidation Catalysts Carrying Non-Innocent Ligands: Mechanistic Insight Through Structure-Activity Relationships and Quantum Chemical Calculations. *Catal. Sci. Technol.* **2016**, *6*, 1306−1319.

(13) (a) Tong, L.; Wang, Y.; Duan, L.; Xu, Y.; Cheng, X.; Fischer, A.; Ahlquist, M. S. G.; Sun, L. Water Oxidation Catalysis: Influence of Anionic Ligands upon the Redox Properties and Catalytic Performance of Mononuclear Ruthenium Complexes. *Inorg. Chem.* **2012**, *51*, 3388−3398. (b) Lu, Z.; Gao, Y.; Chen, H.; Liu, Z.; Chen, L.; Sun, L. Efficient Molecular Ruthenium Catalysts Containing Anionic Ligands for Water Oxidation. *Dalton Trans* **2016**, *45*, 18459−18464.

(14) (a) Lu, Z.; Gao, Y.; Chen, H.; Liu, Z.; Sun, L. Water Oxidation Catalyzed by a Charge-Neutral Mononuclear Ruthenium(III) Complex. *Dalton Trans* **2017**, *46*, 1304−1310. (b) Rabten, W.; Akermark, T.; Karkas, M. D.; Chen, H.; Sun, J.; Andersson, P. G.; Akermark, B. A Ruthenium Water Oxidation Catalyst Based on a Carboxamide Ligand. *Dalton Trans* **2016**, *45*, 3272−3276.

(15) (a) Yoshida, M.; Masaoka, S.; Abe, J.; Sakai, K. Catalysis of Mononuclear Aquaruthenium Complexes in Oxygen Evolution from Water: A New Radical Coupling Path using Hydroxocerium(IV) Species. *Chem. - Asian J.* **2010**, *5*, 2369−2378. (b) Kimoto, A.; Yamauchi, K.; Yoshida, M.; Masaoka, S.; Sakai, K. Kinetics and DFT Studies on Water Oxidation by Ce^{4+} Catalyzed by [Ru(terpy)(bpy)-(OH$_2$)]$^{2+}$. *Chem. Commun.* **2012**, *48*, 239−241. (c) Yoshida, M.; Kondo, M.; Torii, S.; Sakai, K.; Masaoka, S. Oxygen Evolution Catalyzed by a Mononuclear Ruthenium Complex Bearing Pendant SO$_3^-$ Groups. *Angew. Chem., Int. Ed.* **2015**, *54*, 7981−7984.

(16) (a) Wasylenko, D. J.; Ganesamoorthy, C.; Henderson, M. A.; Koivisto, B. D.; Osthoff, H. D.; Berlinguette, C. P. Electronic Modification of the [Ru^{II}(tpy)(bpy)(OH$_2$)]$^{2+}$ Scaffold: Effects on Catalytic Water Oxidation. *J. Am. Chem. Soc.* **2010**, *132*, 16094−16106. (b) Concepcion, J. J.; Tsai, M.-K.; Muckerman, J. T.; Meyer, T. J. Mechanism of Water Oxidation by Single-Site Ruthenium Complex Catalysts. *J. Am. Chem. Soc.* **2010**, *132*, 1545−1557.

(17) Kundu, A.; Khan, S.; Dey, S.; Dutta, C.; Anoop, A.; Mandal, S. Synthesis and Physicochemical Properties of Ruthenium(II) Complexes Having Pentadentate Scaffolds: Water Oxidation Activity and Deactivation Pathway. *Eur. J. Inorg. Chem.* **2019**, *2019*, 164−177.

(18) Shaffer, D. W.; Xie, Y.; Concepcion, J. J. O−O Bond Formation in Ruthenium-Catalyzed Water Oxidation: Single-Site Nucleophilic Attack vs. O−O Radical Coupling. *Chem. Soc. Rev.* **2017**, *46*, 6170− 6193.

(19) Umena, Y.; Kawakami, K.; Shen, J.-R.; Kamiya, N. Crystal Structure of Oxygen-Evolving Photosystem II at a Resolution of 1.9 Å. *Nature* **2011**, *473*, 55−60.

(20) Yamaguchi, K.; Isobe, H.; Yamanaka, S.; Saito, T.; Kanda, K.; Shoji, M.; Umena, Y.; Kawakami, K.; Shen, J. R.; Kamiya, N.; Okumura, M. Full Geometry Optimizations of the Mixed-Valence $CaMn_4O_4X(H_2O)_4$ (X = OH or O) Cluster in OEC of PS II: Degree of Symmetry Breaking of the Labile Mn-X-Mn Bond Revealed by Several Hybrid DFT Calculations. *Int. J. Quantum Chem.* **2013**, *113*, 525−541.

(21) Chatterjee, S.; Singh, P.; Fiedler, J.; Bakova, R.; Zalis, S.; Kaim, W.; Goswami, S. Effect of Metal Exchange (Os vs. Ru) and Co-Ligand Variation (Cl⁻ vs. acac⁻) on the Oxidation State Distribution in Complexes of an o-Phenylenediamido(2-)/o-Quinonediimine Redox System. *Dalton Trans* **2009**, 7778−7785.

(22) Kalyanasundaram, K.; Zakeeruddin, S. M.; Nazeeruddin, M. K. Ligand to Metal Charge Transfer Transitions in Ru(III) and Os(III) Complexes of Substituted 2,2'-Bipyridine. *Coord. Chem. Rev.* **1994**, *132*, 259−264.

(23) Daniel, Q.; Huang, P.; Fan, T.; Wang, Y.; Duan, L.; Wang, L.; Li, F.; Rinkevicius, Z.; Mamedov, F.; Ahlquist, M. S. G.; Styring, S.; Sun, L. Rearranging from 6- to 7-Coordination Initiates the Catalytic Activity: An EPR Study on a Ru-bda Water Oxidation Catalyst. *Coord. Chem. Rev.* **2017**, *346*, 206−215.

(24) Daniel, Q.; Duan, L.; Timmer, B. J. J.; Chen, H.; Luo, X.; Ambre, R.; Wang, Y.; Zhang, B.; Zhang, P.; Wang, L.; Li, F.; Sun, J.; Ahlquist, M.; Sun, L. Water Oxidation Initiated by In Situ Dimerization of the Molecular Ru(pdc) Catalyst. *ACS Catal.* **2018**, *8*, 4375−4382.

(25) Fabre, M.; Bonvoisin, J. Electronic and Magnetic Communication in Mixed-Valent and Homovalent Ruthenium Complexes Containing Phenylcyanamide Type Bridging Ligands. *J. Am. Chem. Soc.* **2007**, *129*, 1434−1444.

(26) Duan, L.; Xu, Y.; Zhang, P.; Wang, M.; Sun, L. Visible Light-Driven Water Oxidation by a Molecular Ruthenium Catalyst in Homogeneous System. *Inorg. Chem.* **2010**, *49*, 209−215.

(27) Mathur, D. L.; Bakore, G. V. Oxidation of sec-Butyl Alcohol by Cerium(IV). *Bull. Chem. Soc. Jpn.* **1971**, *44*, 2600−2602.

(28) Parent, A. R.; Crabtree, R. H.; Brudvig, G. W. Comparison of Primary Oxidants for Water-Oxidation Catalysis. *Chem. Soc. Rev.* **2013**, *42*, 2247−2252.